COMPUTATIONAL CONTINUUM MECHANICS

ВЫЧИСЛИТЕЛЬНАЯ МЕХАНИКА СЛОШНЫХ СРЕД

Computational Continuum Mechanics. 2021. Vol. 14. No. 3. pp. 300-311 DOI: 10.7242/1999-6691/2021.14.3.25

STUDY OF LOCALIZED SHEAR FAILURE OF AMg6 ALLOY SPECIMENS UNDER STATIC AND DYNAMIC LOADING

M.A. Sokovikov[1], M.Yu. Simonov[1,2], V.A. Oborin[1], V.V. Chudinov[1], S.V. Uvarov[1] and O.B. Naimark[1]

[1]*Institute of Continuous Media Mechanics UB RAS, Perm, Russian Federation*
[2]*Perm National Research Polytechnic University, Perm, Russian Federation*

Experiments on dynamic loading of specimens made of AMg6 alloy were conducted on the Hopkinson–Kolsky bar apparatus, while the static loading tests were carried out on the Testometric electromechanical testing machine. Temperature fields generated in the processes of dynamic deformation were investigated "in-situ" by recording temperatures with a high-speed infrared camera CEDIP Silver 450M. The measured temperature in the zone of strain localization under dynamic loading does not confirm the traditional view of the strain localization mechanism due to thermoplastic instability. Static and dynamic tests were carried out for AMg6 alloy specimens specifically designed to study plastic strain localization using the Testometric electromechanical testing machine and split Gopkinson–Kolsky bar, as well as the StrainMaster system for noninvasive measurement of shape and strains. Displacement and strain fields generated in specially shaped AMg6 alloy specimens under static deformation and dynamic loading were constructed. Comparison of the experimentally obtained temperature fields under dynamic loading and strain fields under static and dynamic loading with the results of numerical modeling made with account of kinetics of mesodefect accumulation in the material shows good agreement to the accuracy of ~20%. After the experiments, the surface relief of specially shaped stressed specimens was examined using an optical interferometer-profile meter New View-5010. The processing of the obtained 3D strain relief data made it possible to evaluate the scale invariant (Hurst index) and spatial scale of the area where the correlated behavior of mesodefects was observed. The data of experimental studies, the examination of the surface topography of deformed specimens, structural studies, as well as the data of numerical simulation conducted with consideration of the kinetics of mesodefect accumulation in the material suggest that one of the mechanisms of plastic strain localization in the alloy AMg6 at the examined rates of loading is associated with discontinuous processes in its defect structure. However, the character of specimen failure under static and dynamic loading is due to realization of different scenarios for the behavior of defective subsystems.

Key words: plastic shear localization, dynamic loading, numerical simulation, evolution of the defect structure, study of the surface relief of the deformed samples, structural studies

1. Introduction

The phenomenon of plastic strain localization, that is, the formation of small areas of plastic flow, in which the level of plastic strain is orders of magnitude higher than in the surrounding material, is of theoretical and practical interest. The localization of plastic strain in metals under loading is a complex process that depends on the rate and magnitude of deformation, temperature, and also on the evolution of the material structure. A cycle of papers [1-12] is devoted to the study of this phenomenon.

To date, there are two main concepts of the strain localization mechanism: one considers it as a consequence of thermoplastic instability, which is realized at high strain rates; the other relates it to the structural evolution, which may proceed in a wide range of loading rates. Along with thermoplastic instability, significant contribution is made by structural transitions in the ensembles of mesolevel defects (microshifts and microcracks). The qualitative features of the structure-determined mechanism of plastic shear localization (dynamic recrystallization) are described in [9-11].

The aim of this work is to provide experimental and theoretical verification of the mechanism of plastic stain localization associated with the jump-wise processes in defect material structures [13].

2. Experimental study

A theoretical and experimental study of the mechanisms of plastic strain localization in a material subjected to static deformation and dynamic loading on the split Hopkinson pressure bar (Fig. 1a) was carried out for specimens made of aluminum alloy AMg6 exhibiting the "tendency" to plastic flow instability. The Hopkinson bars and the striker are made of high-strength aging steel. The diameters of the bars and the striker are 25 mm, the length of the striker is 52.33 mm: the striking velocity is 42 m/s.

Email addresses for correspondence: sokovikov@icmm.ru

To study the processes of plastic strain localization in the predominant shear mode under dynamic loading on a split Hopkinson pressure bar, we designed and patented test specimens of special shape (U-shaped) and associated tooling, which ensure the realization of a plane strain state [14]. All sections parallel to the lateral surfaces and the drawing plane (Fig. 1b) are in close stress-strain states, which is confirmed by the results of numerical simulation [15].

In order to identify the characteristic stages of strain localization and development of localized shear fracture under dynamic loading, thermodynamics of the deformation process was studied by "in-situ" recording the temperature fields with a CEDIP Silver 450M high-speed infrared camera (Fig. 1c). The main technical characteristics of the camera are as follows: sensitivity is not less than 25 mK at 300 K, spectral range is 3-5 microns, maximum frame size is 320x240 pixels [15]. The spatial resolution ("pixel size") is ~0.2 mm, and the temporal resolution is ~0.25 ms.

In [15], it was shown that at strain rates of ~10^3 s^{-1} and higher, the characteristic times of thermal conductivity for the AMg6 alloy are much longer than the characteristic times of the deformation process. By studying the temperature fields on the lateral surface in the real time mode, one can get clear understanding of the distributions of temperature fields and plastic strains in all sections of specimens parallel to the lateral surface. The results of the experiments are shown in Figures 1c, d and 2.

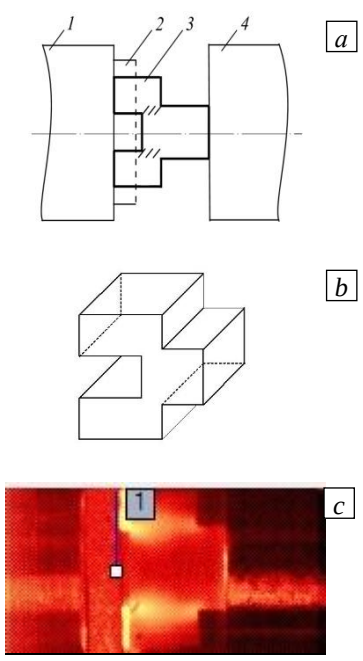

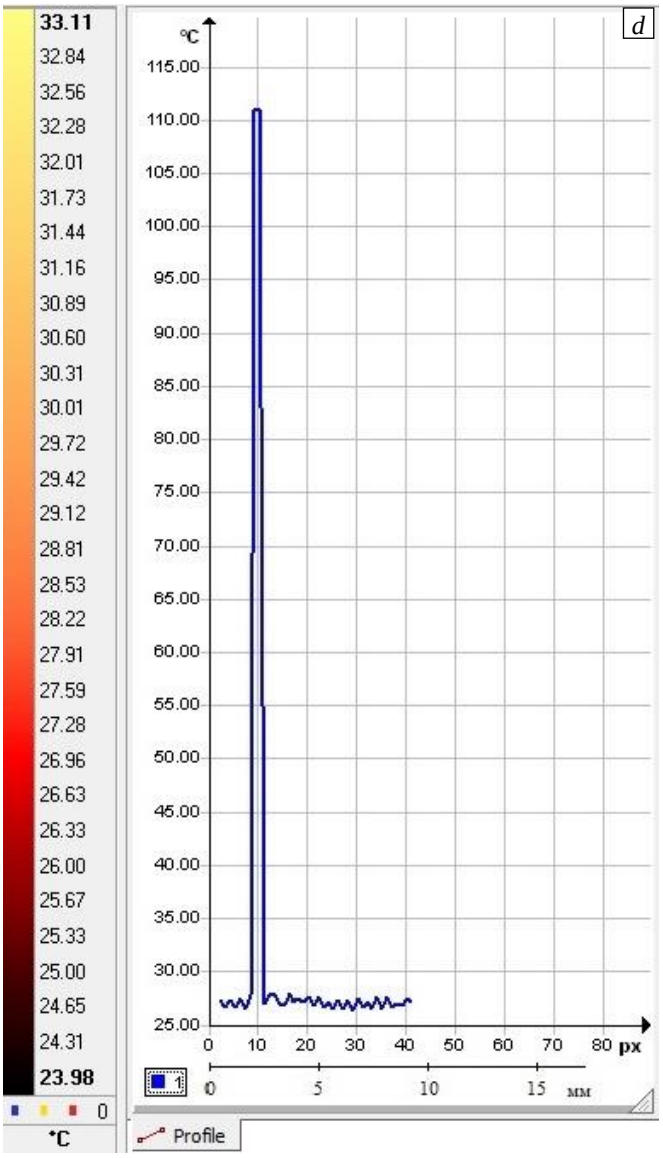

Fig. 1. Scheme of specimen installation between the split Hopkinson bars (a): 1 - input bar, 2 - frame, 3 - specimen (shaded areas are in the predominant shear conditions), 4 - output bar; specimen for tests in the predominant shear conditions (U-shaped) (b); infrared image of the AMg6 alloy specimen during tests in the predominant shear conditions (c); temperature dependence along the coordinate (vertical line in Fig. 1c) at the selected time, the maximum temperature ~110°C (d).

In [15], it was shown that at strain rates of ~10^3 s^{-1} and higher, the characteristic times of thermal conductivity for the AMg6 alloy are much longer than the characteristic times of the deformation process. By studying the temperature fields on the lateral surface in the real time mode, one can get clear understanding of the distributions of temperature fields and plastic strains in all sections of specimens parallel to the lateral surface. The results of the experiments are shown in Figures 1c, d and 2.

The data obtained from the experiments with the infrared camera made it possible to conclude that for AMg6 alloy specimens tested under specified loading conditions at average strain rates of ~5000 s-1 thermal softening does not play a decisive role in the mechanism of shear strain localization. It is this strain rate that was realized when testing with U-shaped specimens. The values of strain rates were obtained from the numerical simulations.

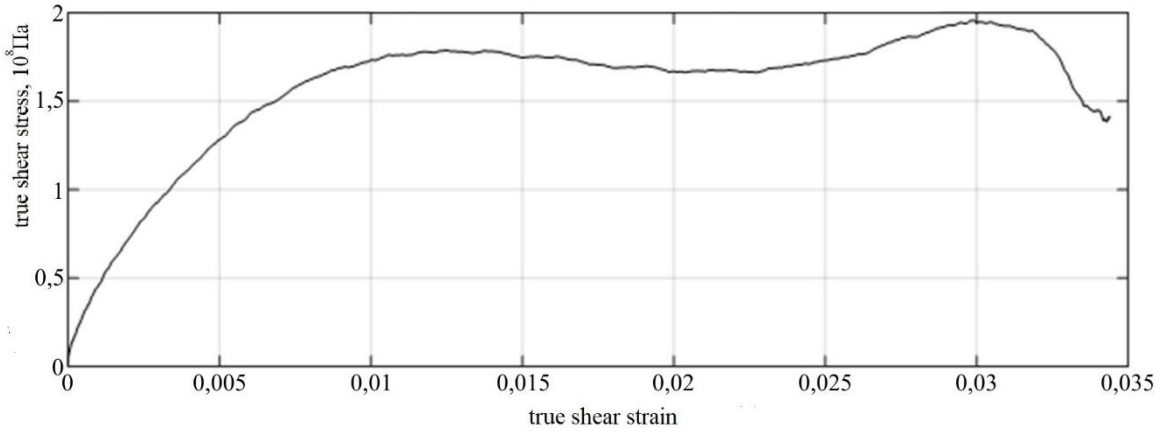

Fig. 2. Diagram of true shear stress as a function of true shear strain obtained as a result of split Hopkinson pressure bar tests of U-shaped AMg6 alloy specimens at striking velocity of 42 m/s.

Additionally, for the AMg6 alloy specimens specifically designed to study plastic strain localization, we determined experimentally the strain fields in the zone of plastic shear localization during static deformation on the electromechanical testing machine Testometric and dynamic loading on the split Hopkinson pressure bar using the StrainMaster system for the noninvasive shape and strain measurements. The error of measurements of the displacement and shear strain fields was ~5%.

During static loading, the displacement and strain fields were determined by the step-frame recording of the mapped points. In the mode of dynamic loading of specimens on the split Hopkinson pressure bar the mapped point patterns were fixed before and after deformation. Then the displacement and strain fields were determined based on the changes in these patterns. The results of the tests are given below.

3. Numerical simulation

A complete system of field equations describing the deformation behavior of the material is written as [15, 16]:

$$\rho\dot{\mathbf{v}} = \nabla\cdot\boldsymbol{\sigma}, \tag{1}$$

$$\dot{\rho} + \rho\nabla\cdot\mathbf{v} = 0, \tag{2}$$

$$\mathbf{D} = \frac{1}{2}\left(\nabla\mathbf{v} + \mathbf{v}\nabla\right), \tag{3}$$

$$\boldsymbol{\sigma}^R = \lambda I_1\left(\mathbf{D}\right) + 2G\left(\mathbf{D} - \mathbf{D}^{pl} - \dot{\mathbf{p}}\right), \tag{4}$$

$$\mathbf{D}^{pl} = \dot{\varepsilon}_0^{n_\varepsilon}\exp\left(\frac{U\left(T\right)}{kT}\right)\left(\Gamma_\sigma\boldsymbol{\sigma} - \Gamma_{p\sigma}\frac{\partial F}{\partial\mathbf{p}}\right), \tag{5}$$

$$\dot{\mathbf{p}} = \dot{\varepsilon}_0^{n_p}\exp\left(\frac{U\left(T\right)}{kT}\right)\left(\Gamma_{p\sigma}\boldsymbol{\sigma} - \Gamma_p\frac{\partial F}{\partial\mathbf{p}}\right), \tag{6}$$

$$\frac{F}{F_m} = \frac{p^2}{2} - \frac{p^2}{2\delta} + c_1 p + c_2\ln\left(c_3 + c_4 p + p^2\right) - \frac{\boldsymbol{\sigma}:\mathbf{p}}{2G}, \tag{7}$$

$$\rho c\dot{T} = \alpha\Delta T + \boldsymbol{\sigma}:\mathbf{D}^{pl} - \frac{\partial F}{\partial\mathbf{p}}:\dot{\mathbf{p}}, \tag{8}$$

$$\dot{\varepsilon}_0 = \frac{\sqrt{(2/3)\dot{\boldsymbol{\varepsilon}}:\dot{\boldsymbol{\varepsilon}}}}{\dot{\varepsilon}_c}, \tag{9}$$

$$\dot{p}_0 = \frac{\sqrt{\dot{\mathbf{p}} : \dot{\mathbf{p}}}}{\dot{\varepsilon}_c}, \tag{10}$$

where (1) are the equations of motion (hereinafter the dot above the symbol means the material derivative), (2) are the continuity equations, (3) is the kinematic relation, (4) is Hooke's law in the framework of velocity formulation, (5), (6) are the kinetic equations, (7) are the expressions for non-equilibrium free energy, (8) are the equations of thermal conductivity, (9) is the expression for the characteristic strain rate. The following notation is used: ρ is the mass density; $\mathbf{v}$ is the velocity vector; $\boldsymbol{\sigma}$ is the stress tensor; $\boldsymbol{\varepsilon}$ is the strain tensor; $\mathbf{D}$ and $\mathbf{D}^{pl}$ are the strain rate tensor and its plastic component; $(\sigma)^R$ is the Green-Nagdi derivative; $I_1(\cdot)$ is the first invariant of the tensor; λ and G is the elastic characteristics of the material; $\mathbf{p}$ is the microshear density tensor; n_p, n_ε are the constants responsible for the velocity sensitivity of the material; $U(T)$ is the characteristic activation energy; T is temperature; k is the Boltzmann constant; Γ_σ, $\Gamma_{p\sigma}$, Γ_p are the kinetic coefficients; F is the nonequilibrium free energy; δ is the structural scaling parameter; F_m, c_1, …., c_4 are the potential approximation constants; c is the specific heat capacity; α is the thermal conductivity coefficient; $\dot{\varepsilon}_c$ is the non-dimensionalization parameter equal to 1 s^{-1}.

The system of equations (1)-(10) describes the deformation behavior of plastic materials (metals and alloys) in the strain rate range of 10^{-4}–10^3 c^{-1} taking into account the defect kinetics and thermal softening. The model parameters were determined by minimizing the discrepancy between the experimental and theoretical strain diagrams at different strain rates. The constants for the AMg6 alloy were determined in earlier studies [15, 16].

Numerical modeling of the split Hopkinson pressure bar (SHPB) testing of the AMg6 alloy specimens was performed using the finite element method. The results of calculations are shown in Fig. 3. The calculated temperature fields developed on the surface of specimens in the process of deformation agree with the experimental data with an accuracy of ~20%.

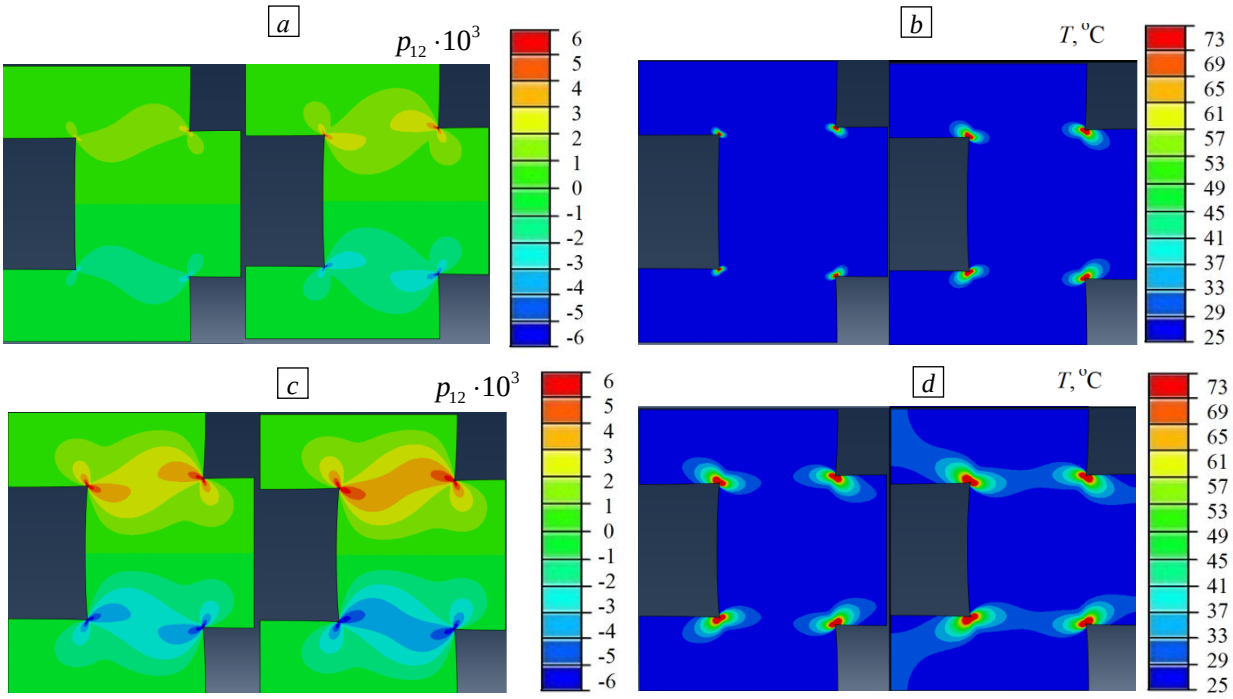

Fig. 3. Evolution of the shear component of microdefect density tensor p_{12} (a), (c) and temperature distribution fields (b), (d) over time $t\times10^5$, c: 1.1 (a), 2.3 (b), 3.5·(c), 4.7(d), when testing the specimen as shown in figure 1 (2D modeling).

The results of numerical simulation of the experiments with AMg6 alloy specimens conducted on the electromechanical testing machine Testometric (under static deformation) and on the split Hopkinson pressure bar (dynamic loading) using the StrainMaster system for noninvasive measurement of the shape and strains

are shown in Figures 4b, 5b. The calculated strain fields agree with the experimental data with an accuracy of ~20%.

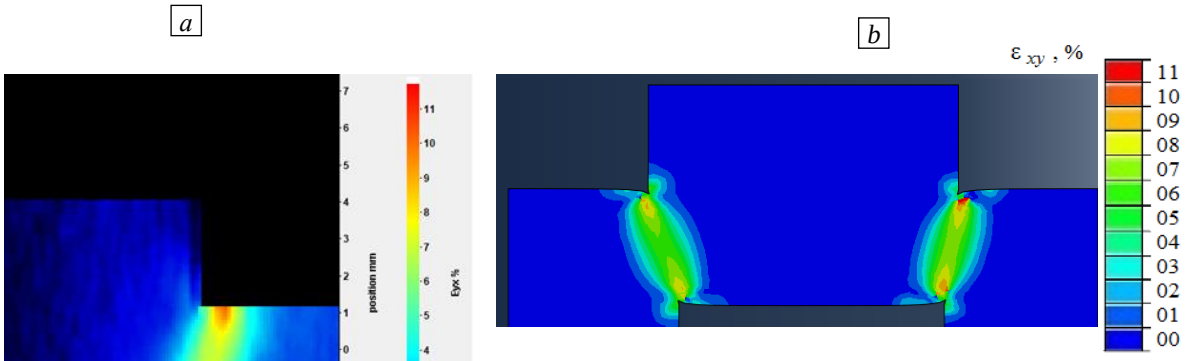

Fig. 4. Distribution of ε_{xy} at the selected moment of time during static loading of U the shaped specimen made of AMg6 alloy: experiment (a), numerical simulation (b).

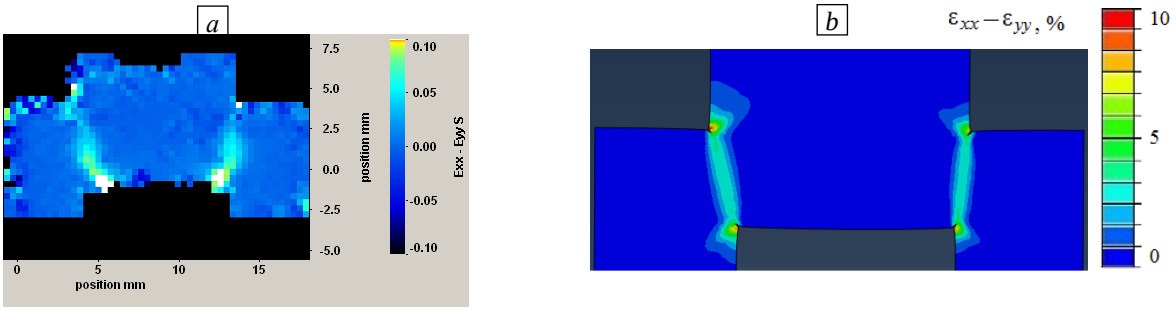

Fig. 5. Distribution of $\left|\varepsilon_{xx}-\varepsilon_{yy}\right|$ at finite time under dynamic loading of the U-shaped specimen made of AMg6 alloy: experiment (a), numerical simulation (b).

4. Study of the deformation relief on the surface of deformed specimens

To verify the theoretical assumptions about the leading role of multiscale mechanisms of structural relaxation caused by the collective behavior of ensembles of defects, and the development of plastic flow and fracture localization, we conducted structural analysis of the surface relief morphology using for this purpose the New View 5010 optical interferometer-profile meter. The obtained data were used to calculate the scale invariant (Hurst exponent) and spatial scale of the area, in which the correlated behavior of microshifts is observed. The evaluation of the Hurst index of defect structures can provide a physical explanation of the generality of critical phenomena observed in the variety of fracture scenarios for different classes of materials and the effect of the structure state (including that formed by dynamic impacts) on the "threshold" characteristics of the material transition from plastic deformation to fracture.

The surface relief of the deformed specimens in the region of maximum shear strain (Fig. 6a) was recorded with a high-resolution New View interferometer-profile meter (at 500X magnification) (Fig. 6b) and then processed, using methods of fractal analysis to determine the conditions of correlated behavior of multiscale defect structures. Within each "window" of size 284x213 μm with vertical resolution of ~0.1 nm and horizontal resolution of ~0.44 μm we examined 12 one-dimensional "slices" to ensure the representativeness of the data of relief structure induced by defects.

Using the one-dimensional profiles of the fracture surface relief (Fig. 6a), the function $K(r)$ is calculated according to the formula from [17]:

$$K(r)=\left\langle \left(z(x+r)-z(x)\right)^2\right\rangle_x^{1/2} \propto r^H ,$$

where $K(r)$ is the average difference in the relief heights $z(x+r)$ and $z(x)$ in the surface window of size r, H is the index of structural scaling (Hurst index).

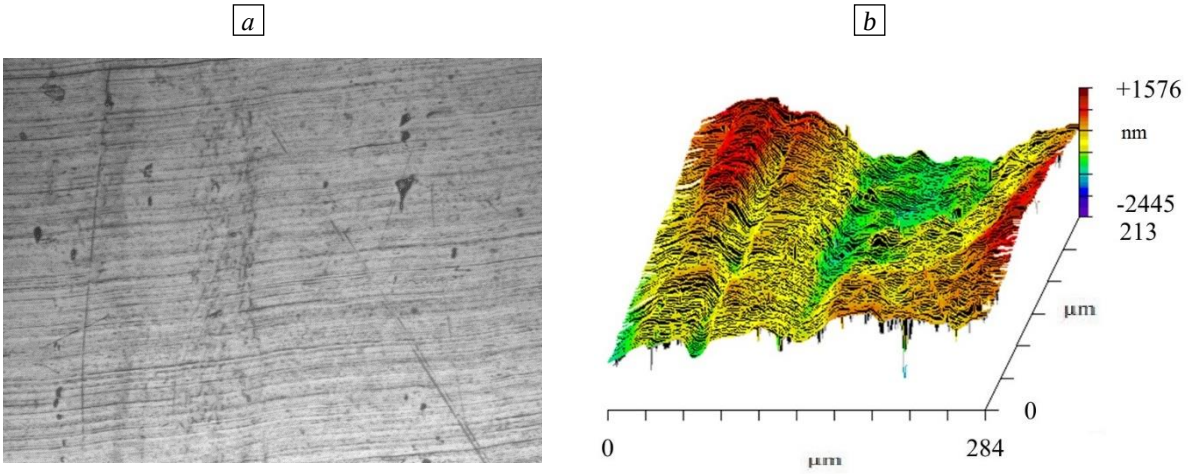

Fig. 6. The surface of specimen No. 4 after dynamic loading: optical view (a) and 3D image (b).

The results of testing the specimens of special shape (surface profile) are shown in Fig. 7a. The representation of the function $K(r)$ in logarithmic coordinates (Fig. 7b) allows us to estimate the Hurst exponent as a spatial invariant in terms of the constant slope of the $\log_2 K(r)$ versus $\log_2 r$ curve in the range of spatial scales from the minimum — l_{sc}, to the maximum — L_{pz}.

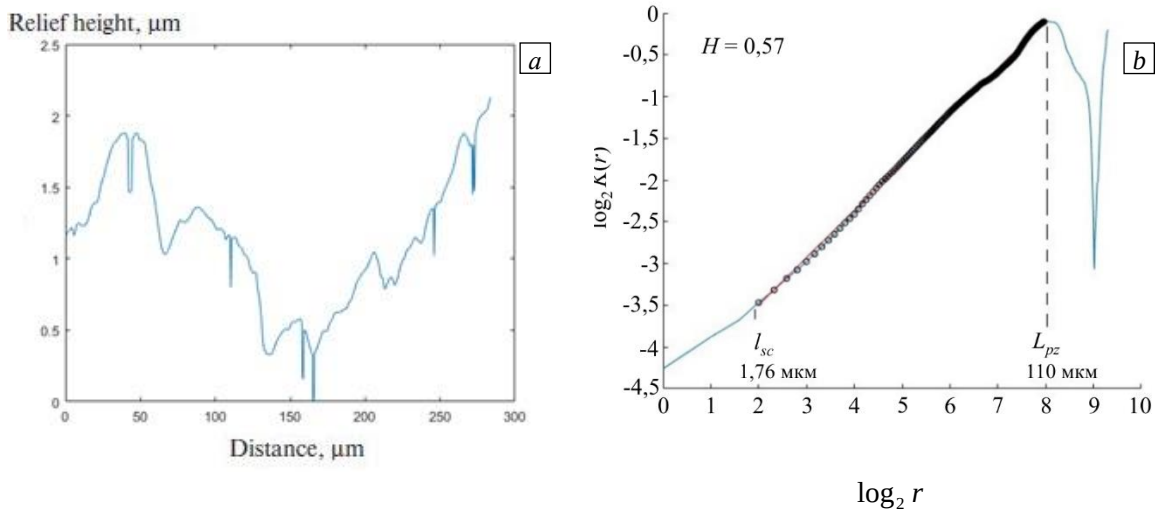

Fig. 7. Characteristic one-dimensional surface profile of specimen No. 4 after deformation (*a*) and the corresponding $\log_2 K(r)$ versus $\log_2 r$ (*b*) curve.

The values of scale invariants and the corresponding structural scales were determined in terms of the Hurst exponent for statically and dynamically loaded specimens (Table 1). It was found that for dynamically deformed specimens there is an increase in the Hurst exponent ($H \sim 0{,}6$) compared to its value in the non-deformed specimens ($H \sim 0{,}5$). The latter is caused by the intensive fragmentation, accompanying the formation of dislocation ensembles in the course of dynamic loading, and is associated with the formation of an ordered system. In compliance with the works of the authors [15], the influence of intensive dynamic loading on the values of scale invariants and spatial scales can be used to study the kinetic regularities of fatigue crack growth and to evaluate the endurance of aircraft engine materials under combined dynamic and fatigue loading.

5. Structural studies

Before metallographic studies, the U-shaped specimens were pressed into conductive bakelite on a CitoPress-10 machine (Struers), then the billets were polished on a Tegramin 30 machine (Struers); distilled water medium was used as lubricant (grease) for rough stripping, and lubricant with highly dispersed silicon oxide particles was used at the final stage. The etching was performed with Keller reagent for 5-10 seconds at 65-70°C.

Table 1. Values of the Hurst index and spatial scales.

Spesimen №*	Before deformation			After deformation		
	H	l_{sc}, μm	L_{pz}, μm	H	l_{sc}, μm	L_{pz}, μm
1*	0,46±0,04	4,2±1,5	66,8±12,4	0,59±0,03	3,0±1,4	41,8±7,7
2*	0,36±0,04	7,1±2,0	30,4±3,4	0,50±0,03	2,3±0,7	85,0±12,3
3*	0,49±0,03	4,4±2,2	34,1±2,3	0,52±0,02	2,8±0,8	29,9±4,4
4**	0,36±0,04	4,6±0,9	20,9±2,3	0,56±0,03	2,7±1,2	103,7±17,7
5**	0,51±0,03	2,9±2,1	42,2±5,9	0,47±0,03	8,1±3,2	57,8±9,7
6**	0,43±0,03	4,2±1,5	46,1±10,7	0,61±0,02	6,6±2,3	83,8±9,2

*Footnote: *specimens are under static loading; *** specimens are under dynamic loading

The electron microscopic studies of the specimen structure were carried out before and after their testing on the electromechanical Testometric machine (static deformation) and on the split Hopkinson pressure bar (dynamic loading). The U-shaped test specimens were crosscut, and the obtained sections were examined and photographed using the FEI PHENOM G2 ProX scanning electron microscope at the accelerating electric field of 15 kV and 2000-15000x magnification.

The initial structure of theAMg6 alloy in specimens No. 1-6 was a set of α - phase grains oriented along the rolling direction. The diameter of grains was about 8-18 microns. The presence of the second phases in the form of cellular conglomerates located in the grain body was observed in all samples.

In what follows is the initial structure of specimens subject to dynamic (Fig. 8) and static tests (Fig. 9).

In all U-shaped specimens, the static and dynamic tests result (to a greater or lesser degree) in the localization of plastic strain in places with peculiarities of geometry. The specimens after tests are shown in Figures 10, 11. Geometric stress concentrators are marked by circles (see Figures 10a and 11a, areas 1-4).

The study of the structure in the areas 1-4 highlighted in Figures 10, 11, allowed us to conclude that the distinguishing characteristic of structuring at medium and maximum loads is the formation of banded structures of localized shear in places of stress concentration due to the specific features of the geometry (see Fig. 12a-e). In Figure 12, the arrows point to the localized shear bands.

An important feature of the formation of localized shear bands after dynamic and static tests at the maximum loading level is the system-based formation of banded structure of crystal clusters. Moreover, in the areas where the banded structure is of cluster character, the localized shear crystals frequently show clear signs of polygonization. The size of polygons does not exceed 1-1.5 μm. In Figure 12c, f, the arrows point to polygons in the localized shear bands.

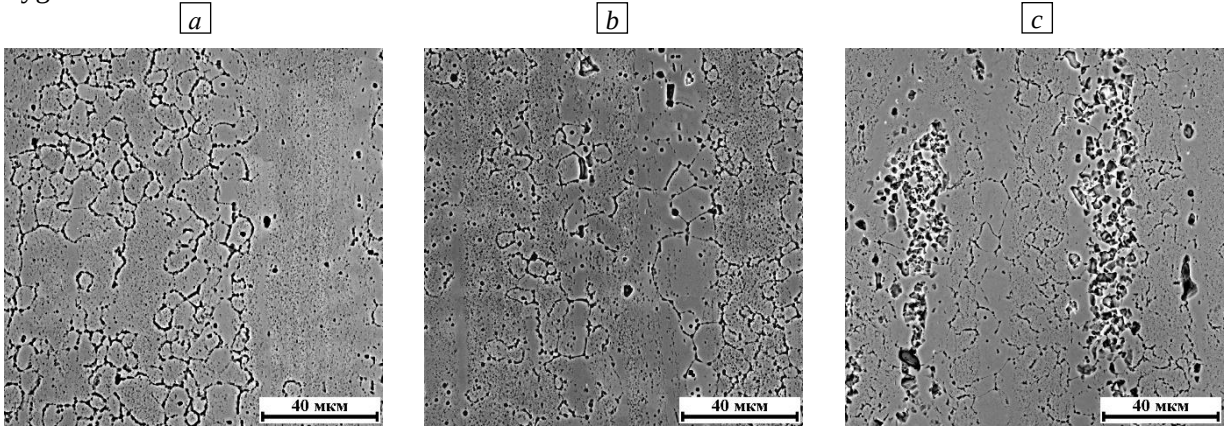

Fig. 8. Initial structure of AMg6 alloy (dynamics); specimens No. 1 (a), (d), (g); specimens No. 2 (b), (e), (h); specimens No. 3 (c), (f), (i); magnification (a)-(c) ×2000, (d)-(f) ×8000, (g)-(i) ×15000.

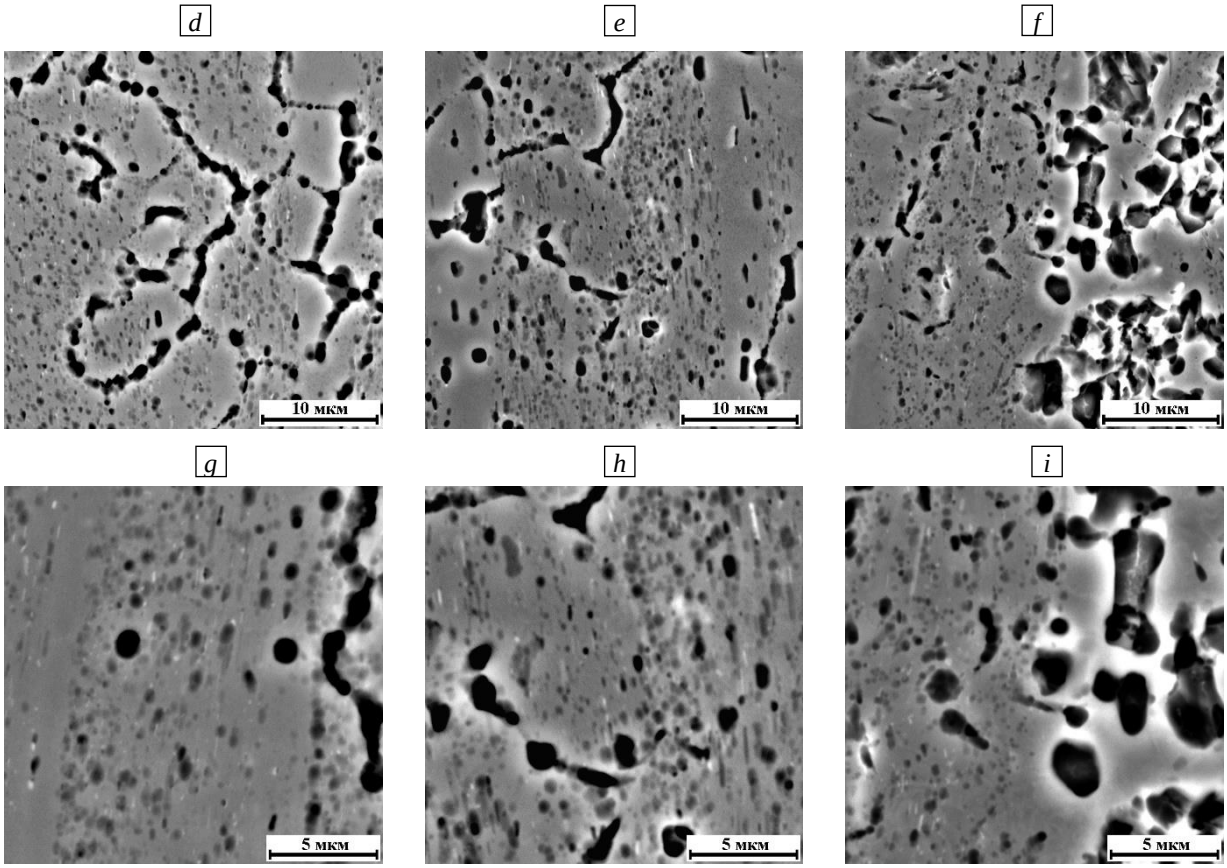

Fig. 8. Continuation.

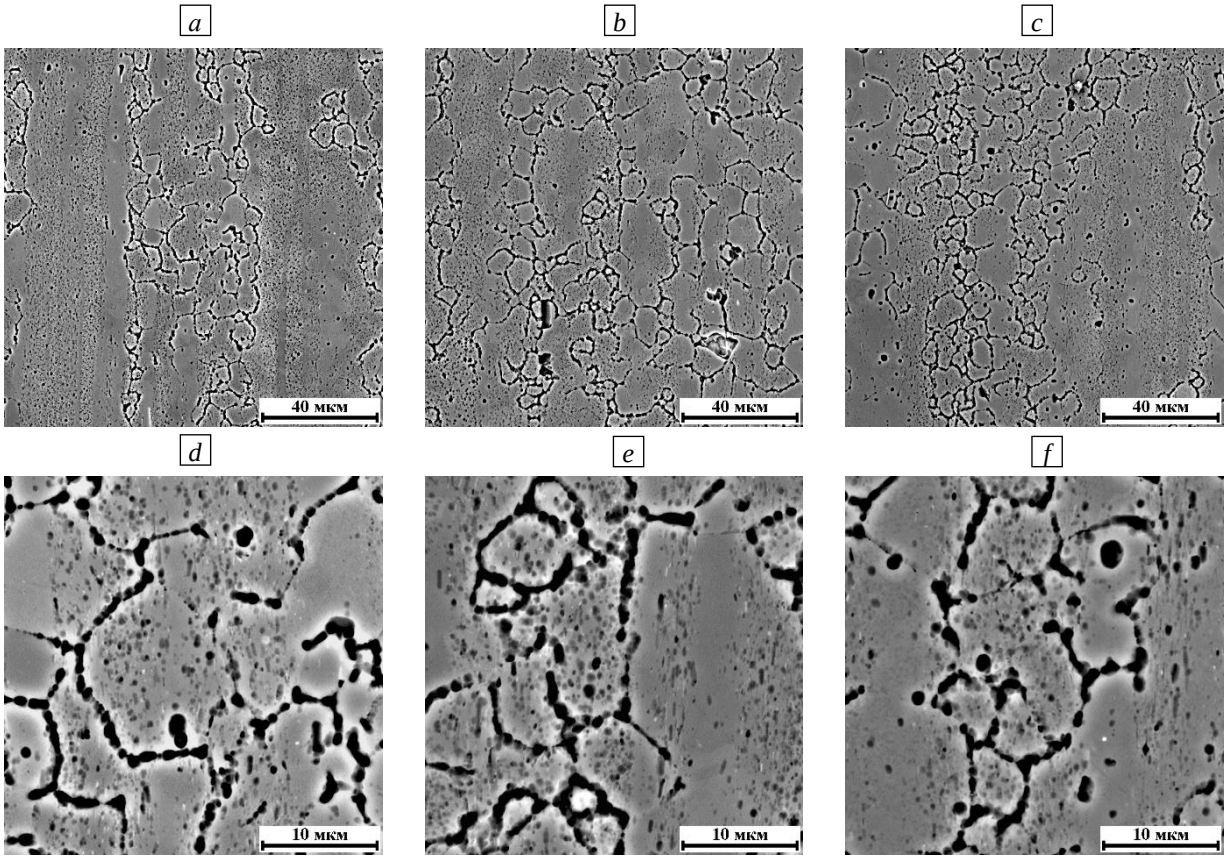

Fig. 9. Initial structure of AMg6 alloy (static); specimen No. 1 (a), (d), (g); specimen No. 2 (b), (e), (h); specimen No. 3 (c), (f), (i); magnification (a)-(c) ×2000, (d)-(f) ×8000, (g)-(i) ×15000.

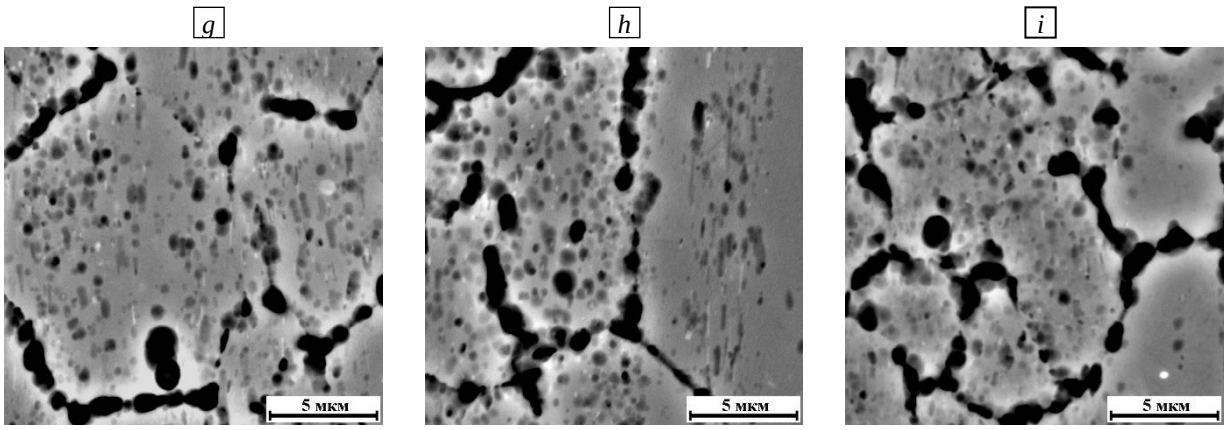

Fig. 9 Continuation.

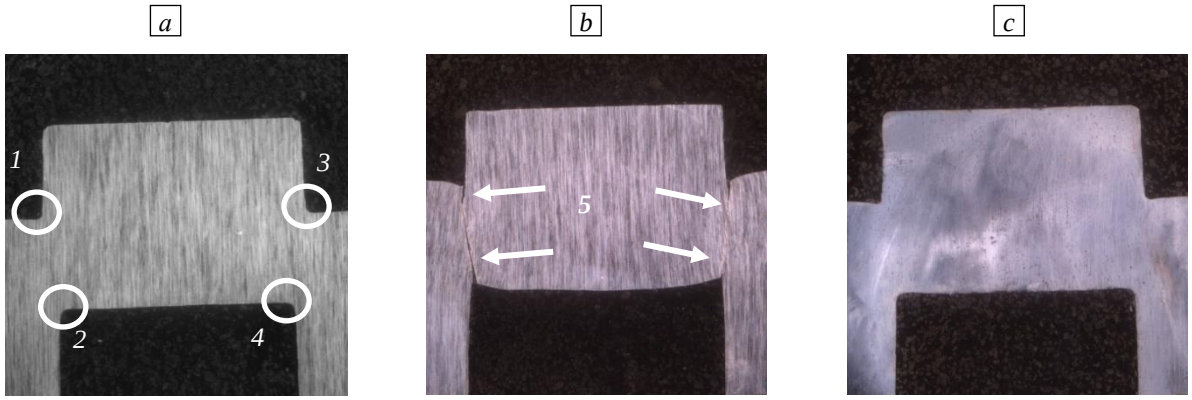

Fig. 10. Fragments of different U-shaped AMr6 alloy specimens after dynamic tests: № 4 (a), № 5 (b) and № 6 (c); areas 1-4 are the locations of plastic strain at the points of geometric stress concentration; 5 - the locations of plastic strain and crosscutting in specimen № 5; magnification is ×20.

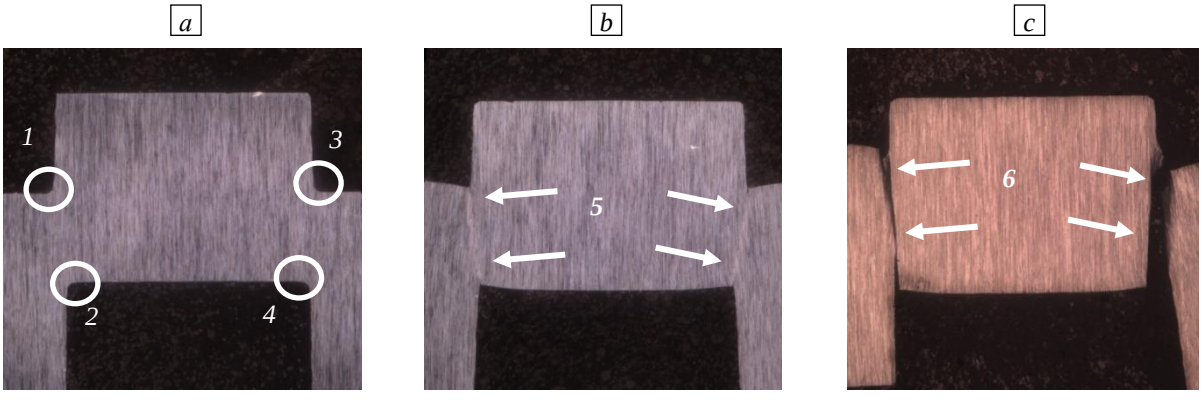

Fig. 11. Fragments of different U-shaped AMr6 alloy specimens after static tests: № 1 (*a)*, № 2 *(b)* and № 3 (*c)*; areas 1-4 are the locations of plastic strain at the points of geometric stress concentration; 5 - the locations of plastic strain in specimen № 2; 6 - locations of detected plastic strain and cutting in specimen No. 3; magnification is ×20.

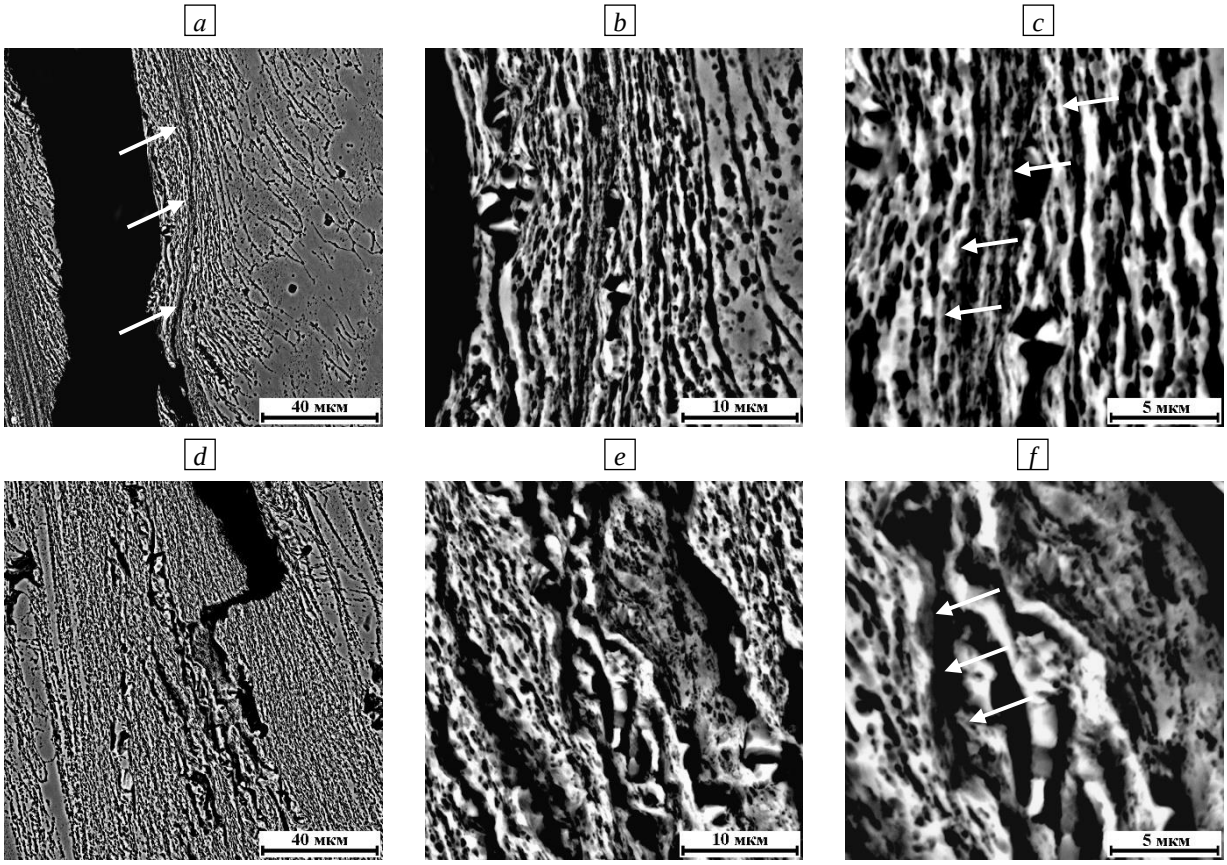

Fig. 12. The structure of plastic strain localization in the areas of geometric stress concentration after dynamic testing of the specimen at maximum loading level (a)-(c) and after static testing (d)-(f); (a)-(f) — area 2 in Fig. 10a: magnification (a), (d)- ×2000; (b), (e)- ×8000; (c), (f)- ×15000.

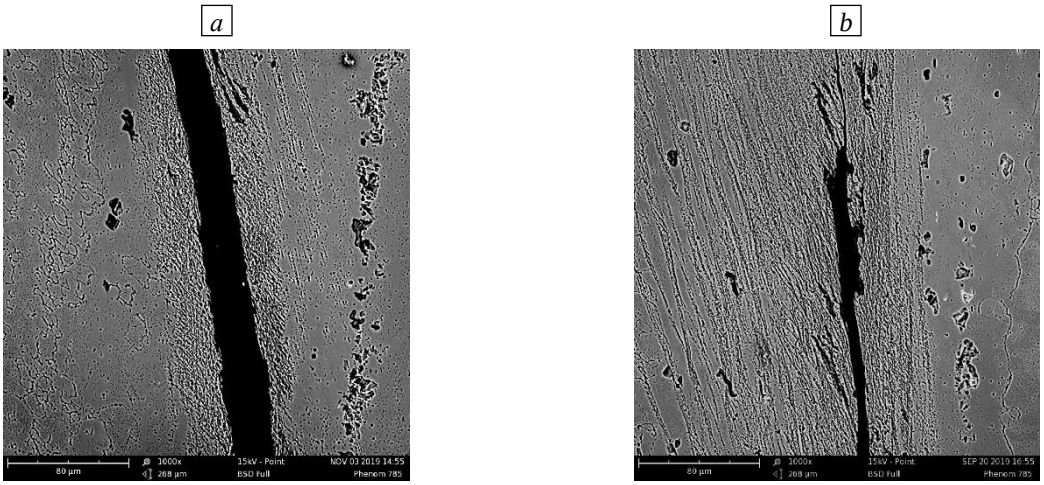

Fig.13. The structure of the AMg6 alloy in the area of deformation band after dynamic (a) and static (b) tests; magnification- ×1000.

It is also worth noting that the localized shear bands formed in the material under maximum dynamic loading occupy smaller area, as opposed to the case of static loading. Thus, in dynamic tests, the width of the area, in which the process of plastic strain localization takes place, is 30-50 μm, while in the direction of the areas with geometric stress concentration (1 and 2, 3 and 4) towards their central point of convergence the width of the area with localized plastic strain enlarges reaching 50-70 μm. In static tests, the width of the area with localized plastic strain is 100-140 μm, while in the direction of the areas with geometric stress concentration (1 and 2, 3

and 4) towards their central point of convergence, the width of area with localization of plastic strain is as large as 250-300 microns and even more. The arrows in Fig. 12 point to the regions of structure, in which the processes of plastic strain localization occur under dynamic (Fig. 13a) and static (Fig. 13b) loading.

5. Conclusion

In this study, using the infrared thermography method and the strain measurement system StrainMaster we investigated the process of plastic strain localization and determined the strain fields of specimens under static and dynamic loading. The obtained results, as well as the data of the numerical simulation done with consideration of kinetics of mesodefect accumulation and the analysis of the surface relief and structure of the deformed specimens made by scanning electron microscope allowed us to suppose that at the realized loading rates one of the mechanisms of plastic strain localization in the AMg 6 alloy is associated with the jump-wise processes in its defect structure. These results also suggest that the character of specimen fracture under realized modes of static and dynamic loading is determined by different scenarios of behavior of the defect subsystems.

The authors would like to thank B.P. Ivanov, Leading Engineer of the IMSS Ural Branch of the Russian Academy of Sciences, for performing the static tests on the Testometric electromechanical machine.

The research was supported by the Russian Science Foundation (Grant №21-79-30041).

References

1. Giovanola H. Adiabatic shear banding under pure shear loading. Part I: direct observation of strain localization and energy dissipation measurements. *Mech. Mater*., 1988, vol. 7, pp. 59-71. https://doi.org/10.1016/0167-6636(88)90006-3
2. Burns T.J. Does a shear band result from a thermal explosion? *Mech. Mater*., 1994, vol. 17, pp. 261-271. https://doi.org/10.1016/0167-6636(94)90064-7
3. Nemat-Nasser S., Li Y.F., Isaacs J.B. Experimental/computational evolution of flow stress at high strain rates with application to adiabatic shear banding. *Mech. Mater*., 1994, vol. 17, pp. 111-134. https://doi.org/10.1016/0167-6636(94)90053-1
4. Bai Y., Xuc Q., Xu Y., Shen L. Characteristics and microstructure in the evolution of shear localization in Ti-6Al-4V alloy. *Mech. Mater.*, 1994, vol. 17, pp. 155-164. https://doi.org/10.1016/0167-6636(94)90056-6
5. Grady D.E. Dynamic of adiabatic shear. *J. Phys. IV France*, 1991, vol. 1, pp. C3-653-C3-660.
6. Belytschko T., Krongauz Y., Organ D., Fleming M., Krysl P. Meshless methods: An overview and recent developments. *Comput. Meth. Appl. Mech. Eng*., 1996, vol. 139, pp. 3-47. https://doi.org/10.1016/S0045-7825(96)01078-X
7. Wright T.W., Ravichandran G. Canonical aspects of adiabatic shear bands. *Int. J. Plast*., 1997, vol. 1, pp. 309-325. https://doi.org/10.1016/S0749-6419(97)80002-2
8. Medyanik S.N., Liu W.K., Li S. On criteria for dynamic adiabatic shear band propagation. *J. Mech. Phys. Solid.*, 2007, vol. 55, pp. 1439-1461. https://doi.org/10.1016/j.jmps.2006.12.006
9. Rittel D., Ravichandran G., Venkert A. The mechanical response of pure iron at high strain rates under dominant shear. *Mater. Sci. Eng.*, 2006, vol. 432, pp. 191-201. https://doi.org/10.1016/j.msea.2006.05.154
10. Rittel D., Wang Z.G., Merzer M. Adiabatic shear failure and dynamic stored energy of cold work. *Phys. Rev. Lett.*, 2006, vol. 96, 075502. https://doi.org/10.1103/PhysRevLett.96.075502
11. Rittel D., Landau P., Venkert A. Dynamic recrystallization as a potential cause for adiabatic shear failure. *Phys. Rev. Lett.*, 2008, vol. 101, 165501. https://doi.org/10.1103/PhysRevLett.101.165501
12. Marchand A., Duffy J. An experimental study of the formation process of adiabatic shear bands in a structural steel. *J. Mech. Phys. Solid.*, 1988, vol. 36, pp. 251-283. https://doi.org/10.1016/0022-5096(88)90012-9
13. Naimark O.B. Collective properties of defects ensembles and some nonlinear problems of plasticity and fracture. *Phys. mesomech.*, 2003, vol. 6, no. 4, pp. 39-63.
14. Naimark O.B., Bayandin Yu.V., Sokovikov M.A., Plekhov O.A., Uvarov S.V., Bannikov M.V., Chudinov V.V. Specimen for shear test (variants) and test method for it. RF Patent No. 2011,114,711/28, Byull. Izobret., 20 May 2013.
15. Bilalov D.A., Sokovikov M.A., Chudinov V.V., Oborin V.A., Bayandin Yu.V., Terekhina A.I., Naimark O.B. Numerical simulation and experimental study of plastic strain localization under the dynamic loading

of specimens in conditions close to a pure shear. *J. Appl. Mech. Tech. Phy.*, 2018, vol. 59, pp. 1179-1188. https://doi.org/10.1134/S0021894418070027

16. Bilalov D.A., Sokovikov M.A., Chudinov V.V. Multiscale mechanisms of plastic strain localization in the process of target perforation. *Deformatsiya i razrusheniye materialov*, 2017, no. 5, pp. 43-47.
17. Bouchaud E. Scaling properties of cracks. *J. Phys.: Condens. Matter.*, 1997, vol. 9, pp. 4319-4344. https://doi.org/10.1088/0953-8984/9/21/002

The authors declare no conflict of interests.
The paper was received on 14.01.2021.
The paper was accepted for publication on 10.06.2021.